IEEE Access
Multidisciplinary ⋮ Rapid Review ⋮ Open Access Journal

Received 15 June 2023, accepted 5 July 2023, date of publication 12 July 2023, date of current version 19 July 2023.

Digital Object Identifier 10.1109/ACCESS.2023.3294407

RESEARCH ARTICLE

Design of H∞ Robust Controller With Load-Current Feedforward for Dual-Active-Bridge DC–DC Converters Considering Parameters Uncertainty

XIAODONG XU [1], **GUANGQING BAO** [2], **YUEWU WANG** [3], **AND QIAN LI** [2]

[1] College of Electrical and Information Engineering, Lanzhou University of Technology, Lanzhou 730050, China
[2] School of Electrical Engineering and Information, Southwest Petroleum University, Chengdu 610500, China
[3] School of Automation, Guangxi University of Science and Technology, Liuzhou 545006, China

Corresponding author: Guangqing Bao (baogq03@163.com)

This work was supported in part by the National Natural Science Foundation of China under Grant 51967012, in part by the Central Government Funds for Guiding Local Scientific and Technological Development of China under Grant 2021ZYD0042, and in part by the Key Research and Development Program of Gansu Province under Grant 20YF8GA055.

ABSTRACT This paper proposes the design of H∞ robust controller with load-current feedforward for dual-active-bridge (DAB) dc-dc converters used in battery energy storage systems, aiming to ensure the dynamic response considering parameters uncertainty that the input voltage varies in a large range and the load is uncertain. Firstly, according to the state-space representation based on dual-phase-shift (DPS) control, a polytopic model of the DAB converter with two uncertain elements is established by convex optimization theory. Based on this model, linear matrix inequalities (LMIs) are then used to design the H∞ robust controller conveniently to minimize the influence of parameters uncertainty disturbance on the output voltage. At the same time, a regional closed-loop pole configuration technique is used to guarantee the dynamic response of the system under a wide range of operating conditions. Furthermore, an improved load-current feedforward control with lookup tables for phase-shift compensation is adopted to further enhance the dynamic response. Finally, an OPAL-RT hardware-in-loop platform with Texas Instruments TMS320F28377D microcontroller is used to verify the feasibility and effectiveness of the proposed H∞ robust controller.

INDEX TERMS Dual-active-bridge (DAB), dual-phase-shift (DPS), H∞controller, load-current feedforward, dynamic response.

I. INTRODUCTION

Benefitting from some advantages such as symmetrical structure, bidirectional power transmission, soft-switching performance, and easy module cascade [1], [2], [3], [4], dual-active-bridge (DAB) dc-dc converter has been widely adopted in industrial applications, such as dc microgrids [5], power electronic transformers [6], distributed generation systems [7], battery energy storage systems (BESS) [8], and medium voltage AC/ DC hybrid power grid [9]. In the above applications, high power density and high efficiency are typical demands for the DAB converter. Especially in BESS, the DAB converter is simultaneously required to guarantee robust dynamic response under parameters uncertainty that the input voltage varies in a large range and the load is uncertain.

In recent years, many control schemes integrated with various phase-shift control strategies have been investigated to ensure the dynamic response of the DAB converter. In an early literature [10], dynamic response comparisons of traditional single-phase-shift (SPS), dual-phase-shift (DPS), and model-based phase-shift control (MPSC) for the DAB

The associate editor coordinating the review of this manuscript and approving it for publication was Vitor Monteiro.

converter are evaluated, with a conclusion that MPSC shows the best dynamic response. In [11], based on SPS control, a load-current feedforward (LCFF) compensation solution is presented to enhance the transient response of the DAB converter against the load change; however, the input voltage fluctuation is not considered. By introducing virtual direct power control (VDPC) into SPS control [12], a VDPC method is proposed to obtain zero overshoot and robust dynamic response when suffering load or input voltage transient disturbances. By combing improved MPSC with LCFF control for the SPS-controlled DAB converter, as presented in [13], the improved strategy can guarantee a faster dynamic response to all the operating ranges. Besides, a discrete extended-phase-shift (EPS) control with low computational complexity is proposed to achieve rapid dynamic response when both load and input voltage change [14]. Moreover, in order to reduce the load current sensor used in the above schemes to lower the hardware cost of the DAB converter, an extended state observer (ESO)-based sensor-reduction control with DPS [15] and a load-current estimating method with switching-period delay compensation [16] are proposed to boost dynamic responses.

Another method for dynamic response improvement for the DAB converter is to engage advanced control schemes, such as model predictive control (MPC), artificial neural network (ANN), sliding mode control, H∞ robust control and linear-quadratic regulator control. Combined with simple SPS, a non-linear MPC with phase-shift compensation is presented to enhance dynamic response against the disturbance of input voltage and load [17]. For DAB converter fast feeding constant power loads or pulsed power loads applied in dc microgrids, an ANN-based MPC method [18], a deep reinforcement learning-based intelligent nonlinear controller [19], an ANN-based active disturbance rejection control with ESO [20], and a moving discretized control set MPC (MDCS-MPC) with SPS [21] are proposed; however, they are extremely complex with a heavy computational burden. In order to lower the computational burden, by utilizing only two prediction horizons, an MDCS-MPC with triple-phase-shift (TPS) is proposed in [22]. Besides, though sliding mode control can provide the DAB converter with a fast transient response for load variations and robust control for parameter uncertainties [23], [24], heavy computation is still an issue. Similar to some advanced control schemes, H∞ robust controller is suited for improving the system stability and performance for power inverters/converters [25], [26], [27], [28], especially when the parameters are uncertain. However, few papers can be found on the application of the DAB converter. To effectively address the system uncertainty and parameter perturbations of the DAB converter, an H∞ mixed sensitivity robust control is presented in [29], which finally obtains a third-order controller by solving Riccati equations, but the selection of the appropriate weighting function is a challenge. Furthermore, To cover such challenges, by using linear matrix inequalities (LMIs) to derive the optimized control parameters, an LMI

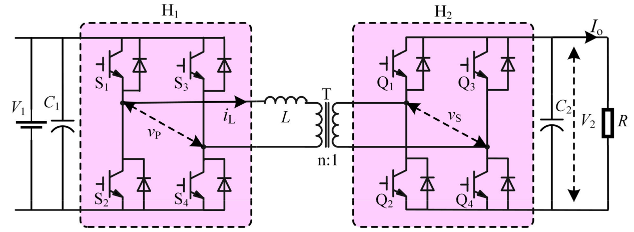

FIGURE 1. Topology configuration of DAB converter.

H∞ robust control is early used to design controllers for boost converters [30], but the disturbance of input voltage is not considered. And then, a robust LMIs-based linear-quadratic regulator control for the DAB converter is improved in [31], which can enhance dynamic performances when both input voltage and load change and achieve robust stability. However, the above two robust controllers in [29] and [31] for the DAB converter are combined with SPS, lacking control freedom compared to DPS, EPS, or TPS.

Thus, in this paper, for more control freedom, based on DPS control, an H∞ robust controller with LCFF for DAB dc-dc converters is proposed, aiming to ensure the dynamic response of the DAB converter considering parameters uncertainty that the input voltage varies in a large range and the load is uncertain. The main contribution of this paper is the establishment of a polytopic model for the DAB converter based on DPS control considering parameters uncertainty, so as to conveniently design the H∞ robust controller by using the LMIs to minimize the influence of parameters uncertainty disturbance on the output voltage. In addition, a regional closed-loop pole configuration technique based on LMIs is used to guarantee the acceptable dynamic response, while an LCFF with lookup tables for phase-shift compensation is improved to further enhance the dynamic response.

This paper is organized as follows. Firstly, a polytopic model of the DAB converter with two uncertain elements is established in Section II. Based on this model, LMIs are then used to design the H∞ robust controller in Section III, with a regional closed-loop pole configuration technique to cope with the system under a wide range of input voltage conditions. Then, an improved LCFF control scheme is adopted to further ensure the dynamic response. Finally, Section IV provides the experimental results obtained from an OPAL-RT hardware-in-loop platform to verify the proposed H∞ robust controller.

II. POLYTOPIC MODEL OF AN UNCERTAIN DAB CONVERTER UNDER DPS CONTROL

A. OPERATION PRINCIPLE AND SMALL-SIGNAL MODEL OF A DAB CONVERTER

Fig. 1 describes the topology of the DAB converter. Two full bridges H_1 and H_2 connect each other with an auxiliary inductor L and an isolated transformer (turn ratio n = 5:8 in this paper). C_1 and C_2 are the dc capacitors. $S_1 \sim S_4$ and

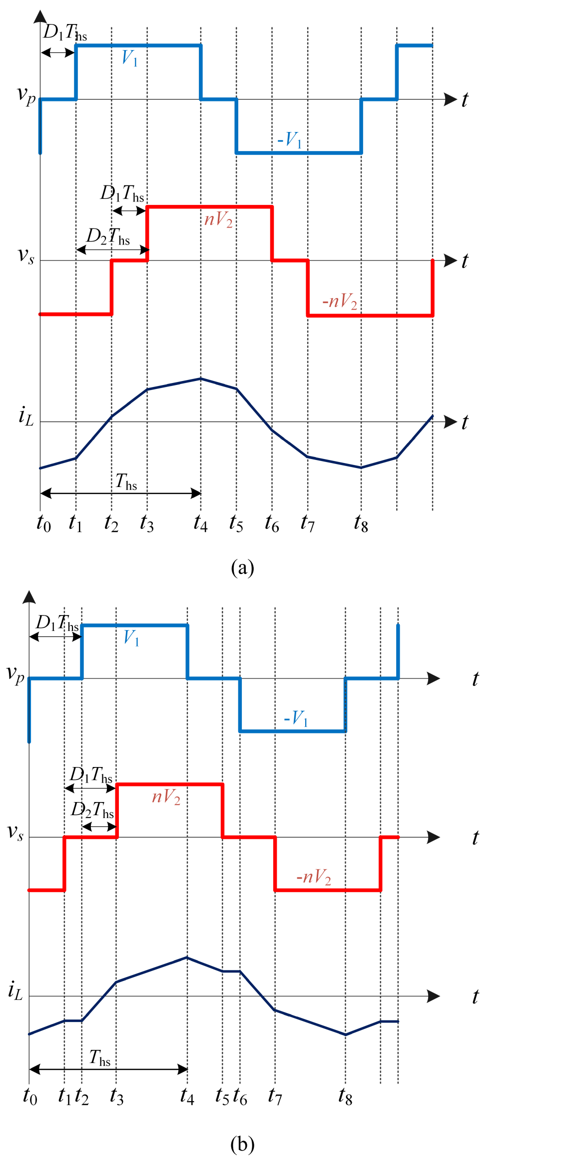

FIGURE 2. **Voltage and current waveforms of DAB converter under DPS control: (a) 0 $\leq D_1 \leq D_2 \leq$ 1, (b) 0 $\leq D_2 \leq D_1 \leq$ 1.**

$Q_1 \sim Q_4$ are two groups of switches in the two full bridges, respectively. V_1 is the dc input voltage, and V_2 is the dc output voltage. v_p and v_s represent the high frequency ac voltages generated by H_1 and H_2, respectively. i_L is the inductor current, and I_o is the load current.

Generally, the DPS-based DAB converter has two degrees of freedom with inner phase-shift ratio and outer phase-shift ratio, which mainly operates in two modes [32]: $0 \leq D_1 \leq D_2 \leq 1$ and $0 \leq D_2 \leq D_1 \leq 1$, as shown in Fig. 2. D_1 represents the inner phase-shift ratio, which is the phase shift between switches S_1 and S_4 or Q_1 and Q_4; D_2 represents the outer phase-shift ratio, which is the phase shift between switches S_1 and Q_1; and T_{1s} is half of the switching cycle. As shown in Fig. 2, under DPS control, the ac voltage output from two full bridges are three-level waves with an equal duty cycle and a specific phase shift. In the existing literature, D_1 is usually used to improve the performances of the DAB converter, such as reactive power [33], current stress [34], and efficiency performance [35]; and D_2 is obtained from a closed-loop control. In this paper, D_1 is directly set to 0.2 for simplicity, so as to focus on the design of proposed H∞ robust controller with D_2.

According to Fig. 1 and Fig. 2, in a switching cycle (T_s), the DAB converter has eight operation modes. Moreover, the inductor current and the ac voltage of the two full bridges show symmetrical waveforms, so the state-space averaging model can be described in half a switching cycle.

In the DAB converter, when the condition meets $0 \leq D_1 \leq D_2 \leq 1$, the inductor current at t_0, t_1, t_2, t_3, t_4 can be described [36]:

$$\begin{cases} i_L(t_0) = \dfrac{V_1}{4f_sL}(D_1 - 1) - \dfrac{nV_2}{4f_sL}(2D_2 + D_1 - 1) \\ i_L(t_1) = \dfrac{V_1}{4f_sL}(D_1 - 1) + \dfrac{nV_2}{4f_sL}(1 + D_1 - 2D_2) \\ i_L(t_2) = \dfrac{V_1}{4f_sL}(2D_2 - D_1 - 1) + \dfrac{nV_2}{4f_sL}(1 - D_1) \\ i_L(t_3) = \dfrac{V_1}{4f_sL}(2D_2 + D_1 - 1) - \dfrac{nV_2}{4f_sL}(D_1 - 1) \\ i_L(t_4) = \dfrac{V_1}{4f_sL}(1 - D_1) + \dfrac{nV_2}{4f_sL}(2D_2 + D_1 - 1) \end{cases} \tag{1}$$

where $f_s = 1/T_s$ is the switching frequency.

As can be seen from Fig. 1 and Fig. 2, it can be obtained four differential equations across the output capacitor C_2 between each time interval of $t_0 \sim t_4$ according to Kirchhoff current law:

$$\begin{cases} C_2\dfrac{dv_2}{dt} = -\bar{i}_{L1} - \dfrac{v_2}{R} & t \in [0, D_1T_{hs}] \\ C_2\dfrac{dv_2}{dt} = -\bar{i}_{L2} - \dfrac{v_2}{R} & t \in [D_1T_{hs}, D_2T_{hs}] \\ C_2\dfrac{dv_2}{dt} = -\dfrac{v_2}{R} & t \in [D_2T_{hs}, (D_1 + D_2)T_{hs}] \\ C_2\dfrac{dv_2}{dt} = -\bar{i}_{L4} - \dfrac{v_2}{R} & t \in [(D_1 + D_2)T_{hs}, T_{hs}] \end{cases} \tag{2}$$

where $\bar{i}_{L1}$, $\bar{i}_{L2}$, and $\bar{i}_{L4}$ represent the inductor current averaging values, which are:

$$\begin{cases} \bar{i}_{L1} = \dfrac{i_L(t_0) + i_L(t_1)}{2} \\ \bar{i}_{L2} = \dfrac{i_L(t_1) + i_L(t_2)}{2} \\ \bar{i}_{L4} = \dfrac{i_L(t_3) + i_L(t_4)}{2} \end{cases} \tag{3}$$

Furthermore, extending the four differential equations in (2) to the entire switching cycle of the DAB converter, time-averaging scheme can be used to derive the final state-space averaging model:

$$C_2\frac{dv_2}{dt} = \frac{nV_1}{4f_sL}[2d_2(1 - d_2) - D_1^2] - \frac{v_2}{R} \tag{4}$$

where d_2 is the outer phase-shift ratio containing ac disturbance.

In order to further derive the small-signal model of the DAB converter, low-frequency ac small-signal disturbance is introduced as

$$\begin{cases} v_2 = V_{2ss} + \hat{v}_2 \\ d_2 = D_{2ss} + \hat{d}_2 \end{cases} \tag{5}$$

where V_{2ss} and D_{2ss} are the dc component of the output voltage and outer phase-shift ratio, respectively, and $\hat{v}_2$ and $\hat{d}_2$ are the corresponding ac components, respectively. Substituting (4) into (5) and ignoring the small-signal ac component $\hat{d}_2^2$, the small-signal model of the DAB converter is derived as

$$\frac{d\hat{v}_2}{dt} = \frac{nV_1}{2f_sLC_2}(1 - 2D_{2ss})\hat{d}_2 - \frac{\hat{v}_2}{RC_2} \tag{6}$$

Aiming to guarantee accurate tracking control for the output voltage, another state variable $x_2(t) = \int \left[V_{ref} - v_2(t)\right] dt$ representing the integral of the corresponding voltage error is introduced. Thus, combining (5) and (6), the state-space representation of the DAB converter is written as

$$\begin{cases} \dot{\boldsymbol{x}}(t) = \boldsymbol{A}\boldsymbol{x}(t) + \boldsymbol{B}_w w(t) + \boldsymbol{B}_u u(t) + \boldsymbol{B}_{ref} V_{ref} \\ z(t) = \boldsymbol{C}_z \boldsymbol{x}(t) + \boldsymbol{D}_{zw} w(t) + \boldsymbol{D}_{zu} u(t) \end{cases} \tag{7}$$

where $\boldsymbol{x}(t) = \begin{bmatrix} v_2(t) \\ x_2(t) \end{bmatrix}$, $w(t) = [i_o(t)]$, $u(t) = [d_2(t)]$, $z(t) = [v_2(t)]$. The vector $\boldsymbol{w}$ represents the disturbance of the load-current i_o. The output z represents the output voltage v_2. Moreover, the state-space matrices are as follows

$$\begin{aligned} &\boldsymbol{A} = \begin{bmatrix} -\frac{1}{RC_2} & 0 \\ -1 & 0 \end{bmatrix}, \quad \boldsymbol{B}_w = \begin{bmatrix} -\frac{1}{C_2} \\ 0 \end{bmatrix}, \\ &\boldsymbol{B}_u = \begin{bmatrix} \frac{nV_1}{2f_sLC_2}(1 - 2D_{2ss}) \\ 0 \end{bmatrix}, \quad \boldsymbol{B}_{ref} = \begin{bmatrix} 0 \\ 1 \end{bmatrix}, \\ &\boldsymbol{C}_z = \begin{bmatrix} 1 & 0 \end{bmatrix}, \quad \boldsymbol{D}_{zw} = [0], \ \boldsymbol{D}_{zu} = [0] \end{aligned} \tag{8}$$

where $\boldsymbol{A}$ is the state matrix; $\boldsymbol{B}_w$ is the disturbance matrix; $\boldsymbol{B}_u$ is the control matrix; $\boldsymbol{B}_{ref}$ is the reference matrix; $\boldsymbol{C}_z$, $\boldsymbol{D}_{zw}$ and $\boldsymbol{D}_{zu}$ are output matrices.

Similarly, when the condition satisfies $0 \le D_2 \le D_1 \le 1$, the state-space averaging model is derived as

$$C_2\frac{dv_2}{dt} = \frac{nV_1}{4f_sL}d_2(2 - 2D_1 - d_2) - \frac{v_2}{R} \tag{9}$$

And the corresponding small-signal model of the DAB converter is derived as

$$\frac{d\hat{v}_2}{dt} = \frac{nV_1}{2f_sLC_2}(1 - D_1 - D_{2ss})\hat{d}_2 - \frac{\hat{v}_2}{RC_2} \tag{10}$$

So as the state-space matrices are obtained as

$$\begin{aligned} &\boldsymbol{A} = \begin{bmatrix} -\frac{1}{RC_2} & 0 \\ -1 & 0 \end{bmatrix}, \quad \boldsymbol{B}_w = \begin{bmatrix} -\frac{1}{C_2} \\ 0 \end{bmatrix}, \\ &\boldsymbol{B}_u = \begin{bmatrix} \frac{nV_1}{2f_sLC_2}(1 - D_1 - D_{2ss}) \\ 0 \end{bmatrix}, \quad \boldsymbol{B}_{ref} = \begin{bmatrix} 0 \\ 1 \end{bmatrix}, \\ &\boldsymbol{C}_z = \begin{bmatrix} 1 & 0 \end{bmatrix}, \quad \boldsymbol{D}_{zw} = [0], \ \boldsymbol{D}_{zu} = [0] \end{aligned} \tag{11}$$

B. POLYTOPIC MODEL CONSIDERING THE UNCERTAINTY OF INPUT VOLTAGE AND LOAD

In BESS, considering that the terminal voltage varies widely during battery charging and discharging and the power transmitted to the dc bus depends on the load, that is, the input voltage V_1 of the DAB converter is not a stable value, and the load is uncertain. Therefore, the polytopic model in convex optimization theory can be adopted to build the system model of the DAB converter so that LMI optimization methods can be easily applied to solve the closed-loop controller [30], [37]. This method ensures system stability at different operating points, as well as optimal immunity to disturbances and transient performance. In modelling, the input voltage and the load are taken as uncertainties, that is, a vector $\boldsymbol{p} = (1/R, V_1)$ is used to include the two uncertain terms, which is constrained in the polytopic model. Thus, for the DAB converter, based on the state-space representation (7), the polytopic model can be formed as.

$$\begin{cases} \dot{\boldsymbol{x}}(t) = \boldsymbol{A}(\boldsymbol{p})\boldsymbol{x}(t) + \boldsymbol{B}_w w(t) + \boldsymbol{B}_u(\boldsymbol{p})u(t) + \boldsymbol{B}_{ref} V_{ref} \\ z(t) = \boldsymbol{C}_z x(t) + \boldsymbol{D}_{zw} w(t) + \boldsymbol{D}_{zu} u(t) \end{cases} \tag{12}$$

where the state-space matrices $\boldsymbol{A}(\boldsymbol{p})$ and $\boldsymbol{B}_u(\boldsymbol{p})$ are determined by uncertain terms grouped in the vector $\boldsymbol{p}$. In this paper, $\boldsymbol{A}(\boldsymbol{p})$ and $\boldsymbol{B}_u(\boldsymbol{p})$ have a linear relationship with each uncertain parameter of vector $\boldsymbol{p}$, respectively.

Generally, the introduced vector $\boldsymbol{p}$ contains N uncertain parameters, that is $\boldsymbol{p} = (p_1, p_2, \ldots, p_N)$. Each uncertain p_i is a bounded parameter, which is constrained within a specific range as

$$p_i \in \left[\underline{p}_i, \bar{p}_i\right] \tag{13}$$

Moreover, the possible values of vector $\boldsymbol{p}$ are hold within a hyperrectangle in the parameter space R^N with $L = 2^N$ vertices $\{v_1, v_2, \ldots, v_N\}$. And the system matrix $[\boldsymbol{A}(\boldsymbol{p}), \boldsymbol{B}_u(\boldsymbol{p})]$ for each vertex v_i corresponds to the extrema of a convex polytope, noted $Co\{G_1, G_2, \ldots, G_L\}$. Therefore, the system matrix $[\boldsymbol{A}(\boldsymbol{p}), \boldsymbol{B}_u(\boldsymbol{p})]$ can be contained as

$$\begin{aligned} [\boldsymbol{A}(\boldsymbol{p}), \boldsymbol{B}_u(\boldsymbol{p})] &\in Co\{G_1, G_2, \ldots, G_L\} \\ &:= \left\{ \sum_{i=1}^{L} \lambda_i G_i, \lambda_i \ge 0, \sum_{i=1}^{L} \lambda_i = 1 \right\} \end{aligned} \tag{14}$$

A detailed description of the convex polytope can be found in [37] and [38].

When specific to this paper for the DAB converter, the input voltage V_1 and the load resistance R are considered uncertainties ($N = 2$), while the rest elements are assumed constant. Thus, the two parameters of vector $\boldsymbol{p} = (1/R, V_1)$ are constrained in the following boundaries:

$$1/R \in \left[1/R_{\max}, 1/R_{\min}\right], \quad V_1 \in [V_{1\min}, V_{1\max}] \tag{15}$$

Furthermore, the polytopic model of the DAB converter established in this paper has $L = 2^N = 4$ vertices that determine the uncertain matrices $\boldsymbol{A}(\boldsymbol{p})$ and $\boldsymbol{B}_u(\boldsymbol{p})$. When the

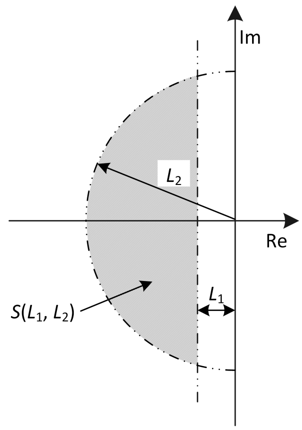

FIGURE 3. **LMI region** $S\,(L_1, L_2)$.

condition meets $0 \leq D_1 \leq D_2 \leq 1$, the vertices are obtained as:

$$
\begin{aligned}
&\boldsymbol{A}_1 = \begin{bmatrix} -\frac{1}{R_{\max}C_2} & 0 \\ -1 & 0 \end{bmatrix}, \quad \boldsymbol{B}_{u1} = \begin{bmatrix} \frac{nV_{1\min}}{2f_sLC_2}(1-2D_{2ss}) \\ 0 \end{bmatrix}, \\
&\boldsymbol{A}_2 = \begin{bmatrix} -\frac{1}{R_{\min}C_2} & 0 \\ -1 & 0 \end{bmatrix}, \quad \boldsymbol{B}_{u2} = \begin{bmatrix} \frac{nV_{1\max}}{2f_sLC_2}(1-2D_{2ss}) \\ 0 \end{bmatrix}, \\
&\boldsymbol{A}_3 = \boldsymbol{A}_2, \quad \boldsymbol{B}_{u3} = \boldsymbol{B}_{u1}, \\
&\boldsymbol{A}_4 = \boldsymbol{A}_1, \quad \boldsymbol{B}_{u4} = \boldsymbol{B}_{u2}
\end{aligned} \tag{16}
$$

III. PROPOSED H∞ ROBUST SOLUTION WITH LOAD-CURRENT FEEDFORWARD

In this section, firstly, H∞ control is adopted to effectively suppress the influence of system parameter perturbation on output and minimize the gain of disturbance on output. Secondly, in order to improve the dynamic settling time of the system, the poles of the closed-loop system are configured in a specific region. In addition, an improved LCFF control is adopted to enhance the dynamic response.

A. H∞ CONTROLLER BASED ON LMIS

For the polytopic model described in (12), there exists a state-feedback controller whose role is to achieve a minimum gain of the disturbance to the output. For the design of robust control systems, the gain of the disturbance to the output is usually transformed into the problem of H∞ norm bound. The H∞ norm can be explained by amplitude-frequency characteristics of a transfer function $f(s)$, which is effective for problems related to model uncertainty. Considering that the transfer function from the disturbance w to the output z is $H(s)$, the corresponding H∞ norm is expressed as

$$
\|H(s)\|_\infty \sup_{w\neq 0} \frac{\|z\|_2}{\|w\|_2} \tag{17}
$$

where $\|\cdot\|_\infty$ represents the infinity norm and $\|\cdot\|_2$ represents the Euclidian norm.

Considering that the smaller the H∞ norm, the better the suppression of the disturbance, when a minimum H∞ norm γ is guaranteed, there exists a state-feedback H∞ controller ($u(t) = d_2(t) = \boldsymbol{K}x(t)$) if and only if a positive definite matrix $\boldsymbol{W} \in \boldsymbol{R}^{n\times n}$ and a matrix $\boldsymbol{Y} \in \boldsymbol{R}^{n\times n}$ make the following LMI hold

$$
\begin{bmatrix} \boldsymbol{AW}+\boldsymbol{WA}^{\mathrm{T}}+\boldsymbol{B}_u\boldsymbol{Y}+\boldsymbol{Y}^{\mathrm{T}}\boldsymbol{B}_u^{\mathrm{T}} & \boldsymbol{B}_w & \boldsymbol{WC}_z^{\mathrm{T}}+\boldsymbol{Y}^{\mathrm{T}}\boldsymbol{D}_{zu}^{\mathrm{T}} \\ \boldsymbol{B}_w^{\mathrm{T}} & -\gamma\boldsymbol{I} & 0 \\ \boldsymbol{C}_z\boldsymbol{W}+\boldsymbol{D}_{zu}\boldsymbol{Y} & 0 & -\gamma\boldsymbol{I} \end{bmatrix} < 0 \tag{18}
$$

Thus, the H∞ controller is obtained by $\boldsymbol{K} = \boldsymbol{YW}^{-1}$. Proof of (18) can be found in [39]. For all the vertices $\{G_1, G_2, \ldots, G_L\}$ in the polytopic model of the DAB converter, it is sufficient to satisfy (18) to solve the stability problem for different steady-state operating points of the system.

B. POLE PLACEMENT LMIS

In the classical control theory, the amplitude-frequency and phase-frequency characteristics of the open-loop system are obtained through the transfer function so as to design the controller according to the Bode diagram. However, the classical control method usually assigns the closed-loop poles precisely, which is not suite for the system with the imprecision of the model and the existence of various disturbances.

Thus, in this paper, LMI is used to directly assign the closed-loop poles of the system in a given region of the complex plane to ensure some desired dynamic characteristics, such as decay rate, settling time, damping ratio, etc. As shown in Fig. 3, in the region $S\,(L_1, L_2)$ of the complex plane for the system [40], the assigned closed-loop poles $(x \pm \mathrm{j}y)$ should meet

$$
x < -L_1 < 0, \quad |x \pm \mathrm{j}y| < L_2 \tag{19}
$$

where L_1 and L_2 are two values given by the designer. L_1 is used to determine a minimum decay rate, and L_2 is used to limit a maximum natural frequency.

Considering the decay rate constrained by L_1, the following LMI is obtained

$$
\boldsymbol{AW} + \boldsymbol{WA}^{\mathrm{T}} + \boldsymbol{B}_u\boldsymbol{Y} + \boldsymbol{Y}^{\mathrm{T}}\boldsymbol{B}_u^{\mathrm{T}} + 2L_1\boldsymbol{W} < 0 \tag{20}
$$

Furthermore, the constraint of the natural frequency according to L_2 involves the following LMI

$$
\begin{bmatrix} -L_2\boldsymbol{W} & \boldsymbol{WA}^{\mathrm{T}}+\boldsymbol{Y}^{\mathrm{T}}\boldsymbol{B}_u^{\mathrm{T}} \\ \boldsymbol{AW}+\boldsymbol{B}_u\boldsymbol{Y} & -L_2\boldsymbol{W} \end{bmatrix} < 0 \tag{21}
$$

A detailed explanation of LMIs (20) and (21) can be found in [40], and it is proven in [40] that when the system with the H∞ robust controller $u\,(t) = d_2\,(t) = \boldsymbol{K}x(t) = \boldsymbol{YW}^{-1}x(t)$ meets LMIs (20) and (21), the closed-loop poles $(x \pm \mathrm{j}y)$ can be directly assigned in the given region $S\,(L_1, L_2)$.

Here, in this paper, all the vertices $\{G_1, G_2, \ldots, G_L\}$ in the polytopic model of the DAB converter need to satisfy LMIs not only (18) but also (20) and (21), so that the closed-loop poles of the system under different stable operating points are

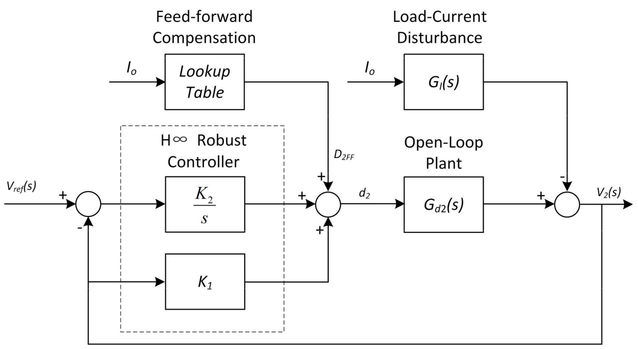

FIGURE 4. H∞ robust control with load-current feedforward compensation for DAB converter.

TABLE 1. Lookup tables for load-current feedforward compensation.

Input Voltage	250 V	300 V	350 V	400 V	450 V
$0 \leqslant D_1 \leqslant D_2 \leqslant 1$	0.0202	0.0169	0.0144	0.0126	0.0112
$0 \leqslant D_2 \leqslant D_1 \leqslant 1$	0.0171	0.0143	0.0122	0.0107	0.0095

assigned in the given region $S(L_1, L_2)$ to meet the acceptable dynamic performance of the system.

Thus, by combining LMIs (18), (20) and (21), the LMI synthesis method for the proposed H∞ robust controller with pole placement can be summarized as the following optimization problem:

$$\begin{cases} \min\limits_{Y,\,W} \quad \gamma \quad \text{subject to (18), (20) and (21)} \\ \qquad\qquad \forall \{G_i\}, \quad i = 1, \ldots, L \end{cases} \tag{22}$$

The solving procedure of the optimization problem (22) consists of finding a set of common matrices $\boldsymbol{Y}$ and $\boldsymbol{W}$ by solving LMIs, so as to obtain the H∞ robust controller $u(t) = d_2(t) = \boldsymbol{K}x(t) = \boldsymbol{Y}\boldsymbol{W}^{-1}x(t)$, which assigns the closed-loop poles of the system in the region $S(L_1, L_2)$ and guarantees a minimum H∞ norm γ.

C. LOAD-CURRENT FEEDFORWARD

In this section, an improved LCFF control is adopted to further enhance the dynamic response of the DAB converter, which treats the load-current as a feedforward compensation to the H∞ robust controller without impact on the design of the controller. Such an idea applied to a DAB converter with SPS control was early proposed in [11], where feedforward compensation was adopted to feed forward a phase shift correction to regulate the output voltage when the load-current changes. In this paper, a similar concept is adopted to cope with the uncertainties of the load resistance with DPS control.

To implement feedforward compensation, a relationship between the load-current and the commanded outer phase-shift ratio D_2' needs to be derived. According to the basic analysis of the DAB converter expressed in [34], the average transmission power with DPS control can be rewritten as

$$P = \begin{cases} \dfrac{nV_1V_2}{2f_sL}\left[D_{2ol}^*(1 - D_{2ol}^*) - \dfrac{D_1^2}{2}\right], \\ \qquad 0 \le D_1 \le D_{2ol}^* \le 1 \\ \dfrac{nV_1V_2}{2f_sL}\left[D_{2ol}^*(1 - D_1) - \dfrac{(D_{2ol}^*)^2}{2}\right], \\ \qquad 0 \le D_{2ol}^* \le D_1 \le 1 \end{cases} \tag{23}$$

where D_{2ol}^* is an open-loop commanded outer phase-shift ratio.

Thus, the load-current can be derived as

$$I_o = \begin{cases} \dfrac{nV_1}{2f_sL}\left[D_{2ol}^*(1 - D_{2ol}^*) - \dfrac{1}{2}D_1^2\right], \\ \qquad 0 \le D_1 \le D_{2ol}^* \le 1 \\ \dfrac{nV_1}{2f_sL}D_{2ol}^*(1 - D_1 - \dfrac{1}{2}D_{2ol}^*), \\ \qquad 0 \le D_{2ol}^* \le D_1 \le 1 \end{cases} \tag{24}$$

It can be seen from (24) that the relationship between the outer phase-shift ratio and the load-current is nonlinear, resulting in complicated inverting. However, for a certain input voltage V_1, one-to-one correspondence between the ideal outer phase-shift ratio $D_{2ol}^* = D_{2FF}$ and any load-current I_o can be precalculated as lookup tables, according to the condition $0 \le D_1 \le D_{2ol}^* \le 1$ or $0 \le D_{2ol}^* \le D_1 \le 1$. Considering that the input voltage ranges from 250 V to 450 V, the lookup tables are established every 50 V for a trade-off. Moreover, for a measured input voltage within the divided interval, a linear interpolation processing is adopted to calculate the target feedforward phase-shift compensation from the two adjacent lookup tables. Thus, in every control interrupt cycle, the controller can look up and calculate the new feedforward compensation for the next control cycle. Fig. 4 shows the block diagram of LCFF compensation implemented in an H∞ robust controller of the DAB converter. According to (24), the lookup tables are calculated and presented in Table 1.

TABLE 2. DAB converter parameters in the HIL setup.

Symbol	Quantity	Value
P_{rated}	Converter Rated Power	5 kW
V_1	Input Voltage	250 V ~ 450 V
V_2	Output Voltage	400 V
f_s	Switching Frequency	2 kHz
D_1	Inner Phase-shift Ratio	0.2
n	Transformer Turn Ratio	5:8
L	Auxiliary Inductor Inductance	500 uH
C_1, C_2	DC Capacitance	1000 uF
$R_{\min}$, $R_{\max}$	Load Resistance	32 Ω ~ 1000 Ω

IV. EXPERIMENTAL VERIFICATION

To verify the proposed design of H∞ robust controller, a real-time hardware-in-the-loop (HIL) platform is established. The

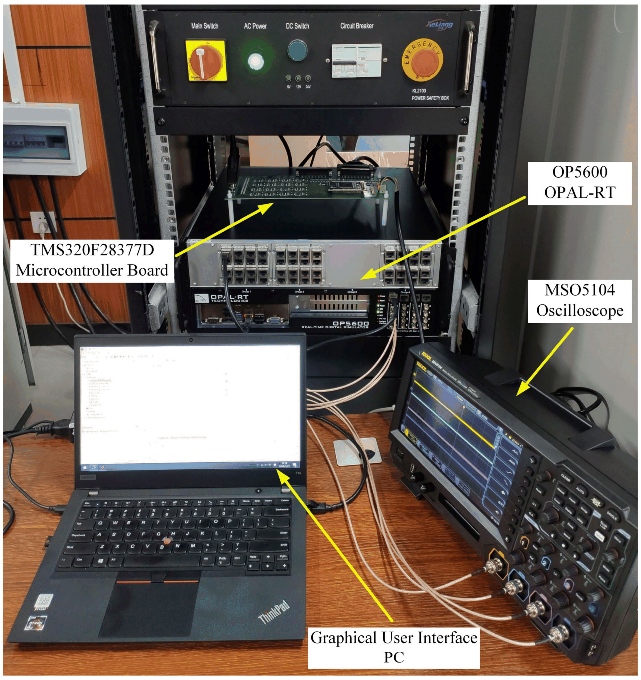

FIGURE 5. OPAL-RT real-time HIL platform with TMS320F28377D microcontroller board.

HIL setup is presented in Fig. 5, consisting of an OPAL-RT OP5600 real-time simulator and a powerful Texas Instruments TMS320F28377D Delfino microcontroller board. The DAB converter is built in the OP5600, and the proposed H∞ robust controller is implemented in the TMS320F28377D. The detailed parameters of the DAB converter in the HIL setup are presented in Table 2.

A. H∞ CONTROLLER DESIGN

The control objective of the system is to obtain a minimum H∞ norm γ by assigning the closed-loop poles within the given region $S(L_1, L_2)$ according to solving the optimization problem (22). In this paper, considering the minimum decay rate and the maximum natural frequency of the system, L_1 can be set to 120, while L_2 can be set to 1/20 of the switching frequency.

When the condition meets $0 \leq D_1 \leq D_2 \leq 1$, by combining the detailed parameters in Table 2, the four vertices in the polytopic model of the DAB converter shown in (16) are calculated as

$$\begin{aligned} \boldsymbol{A}_1 &= \begin{bmatrix} -1 & 0 \\ -1 & 0 \end{bmatrix}, \quad \boldsymbol{B}_{u1} = \begin{bmatrix} 46875 \\ 0 \end{bmatrix}, \\ \boldsymbol{A}_2 &= \begin{bmatrix} -31.25 & 0 \\ -1 & 0 \end{bmatrix}, \quad \boldsymbol{B}_{u2} = \begin{bmatrix} 115310 \\ 0 \end{bmatrix}, \\ \boldsymbol{A}_3 &= \boldsymbol{A}_2, \quad \boldsymbol{B}_{u3} = \boldsymbol{B}_{u1}, \\ \boldsymbol{A}_4 &= \boldsymbol{A}_1, \quad \boldsymbol{B}_{u4} = \boldsymbol{B}_{u2} \end{aligned} \tag{25}$$

Then, the remaining disturbance matrix $\boldsymbol{B}_w$ is calculated as

$$\boldsymbol{B}_w = \begin{bmatrix} -1000 \\ 0 \end{bmatrix} \tag{26}$$

Here, all the parameters and matrices used to solve the optimization problem (22) are obtained. With the help of MATLAB LMI toolbox, a total amount of fourteen LMIs can be formulated by introducing every vertex into (18), (20) and (21). The fourteen formulated LMIs consist of four LMIs from (18), four LMIs from (20), four LMIs from (21), one LMI from positive H∞ norm γ, and one LMI from positive definite matrix $\boldsymbol{W}$.

Take the LMIs of (18) for example, when the first vertex $[\boldsymbol{A}_1, \boldsymbol{B}_{u1}]$ is introduced, the corresponding formulated LMI with MATLAB commands is expressed as

```
lmiterm([1 1 1 W],A1,1,'s');
lmiterm([1 1 1 Y],Bu1,1,'s');
lmiterm([1 1 2 0],Bw);
lmiterm([1 1 3 W],1,Cz');
lmiterm([1 1 3 Y],1,Dzu');
lmiterm([1 2 2 gama],-1,1);
lmiterm([1 3 3 gama],-1,1);
```

Thus, solving the optimization problem (22) by using MATLAB LMI toolbox, a set of common matrices $\boldsymbol{Y}$ and $\boldsymbol{W}$ can be found, obtaining the H∞ controller $\boldsymbol{K}$ as

$$\boldsymbol{K} = \begin{bmatrix} K_1 & K_2 \end{bmatrix} = \begin{bmatrix} 0.0061 & 0.7969 \end{bmatrix} \tag{27}$$

and the H∞ norm is $\gamma = 6.9393$ (also known as 16.83 dB). The control law $u(t) = d_2(t) = \boldsymbol{K}x(t)$ to yield the outer phase-shift ratio can be expressed as

$$d_2(t) = 0.0061v_2(t) + 0.7969x_2(t) \tag{28}$$

Similarly, when the condition meets $0 \leq D_2 \leq D_1 \leq 1$, the control law to yield the outer phase-shift ratio can be obtained as

$$d_2(t) = 0.0071v_2(t) + 0.9491x_2(t) \tag{29}$$

B. EXPERIMENTAL RESULTS

Fig. 6 shows the steady-state experimental waveforms under the proposed H∞ robust controller when the primary side dc voltage V_1 is 250 V. It is clear that the secondary side dc voltage V_2 can be regulated at the designed 400 V under both half-load (R = 64 Ω) and full-load (R = 32 Ω). The full-bridge voltages v_p and v_s are high-frequency three-level waves with the effect of the inner phase-shift ratio, but the outer phase-shift ratio between v_p and v_s has a larger value under full-load in Fig. 6(b) compared with half-load in Fig. 6(a), due to more power needs to be transmitted under full-load.

Under the same load conditions, Fig. 7 shows the steady-state experiment waveforms under the proposed controller while the primary side dc voltage V_1 is set to 450 V. According to Fig. 7, The secondary side dc voltage V_2 is still regulated at the designed 400 V, and the outer phase-shift ratio has a larger value under full-load, while the waveforms of the auxiliary Inductor current i_L become triangle-like instead of trapezoid-like in Fig. 6, with higher peak values.

Fig. 8 shows the dynamic-state experimental comparison of the DAB converter under conventional and proposed

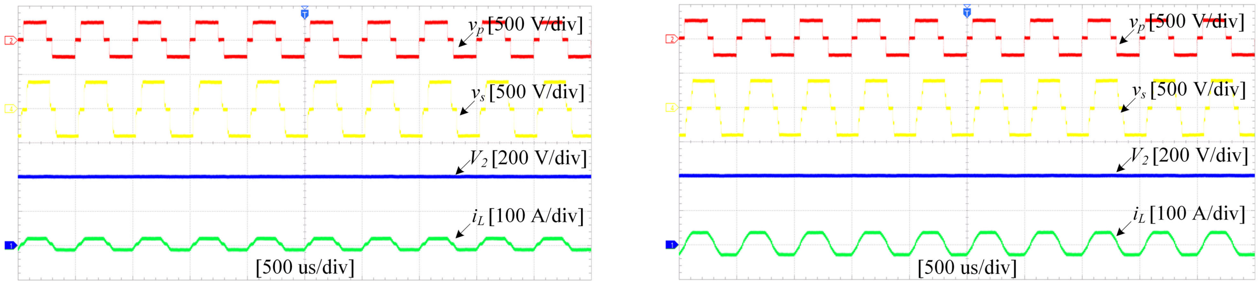

(a) (b)

FIGURE 6. Steady-state experimental waveforms of DAB converter under the proposed controller when the primary side dc voltage is 250 V: (a) Half-load (R = 64 Ω), (b) Full-load (R = 32 Ω).

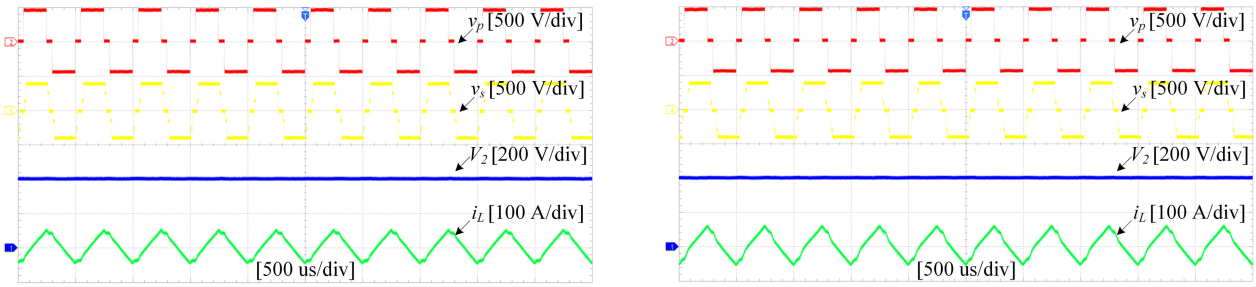

(a) (b)

FIGURE 7. Steady-state experimental waveforms of DAB converter under the proposed controller when the primary side dc voltage is 450 V: (a) Half-load (R = 64 Ω), (b) Full-load (R = 32 Ω).

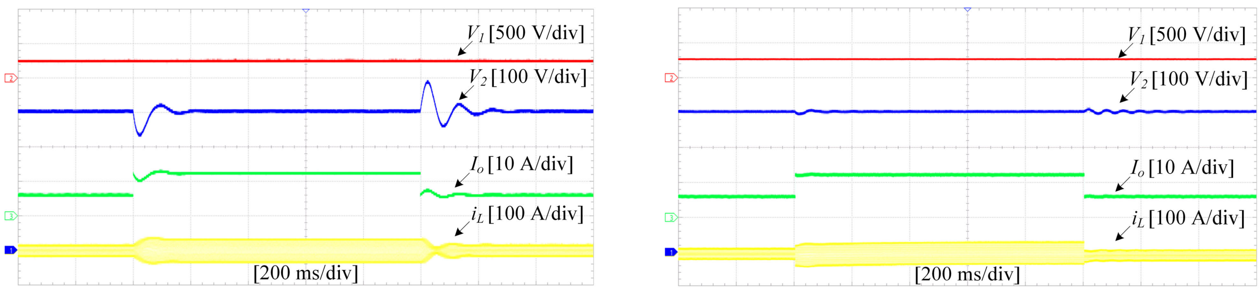

(a) (b)

FIGURE 8. Dynamic-state experimental comparison of DAB converter under conventional and proposed controllers when the primary side dc voltage is 250 V: (a) Conventional controller with load switching between half-load (R = 64 Ω) and full-load (R = 32 Ω), (b) Proposed controller with load switching between half-load (R = 64 Ω) and full-load (R = 32 Ω).

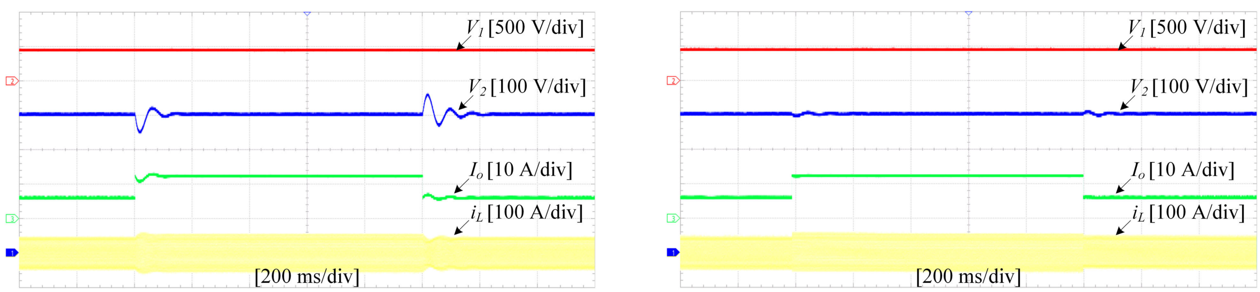

(a) (b)

FIGURE 9. Dynamic-state experimental comparison of DAB converter under conventional and proposed controllers when the primary side dc voltage is 450 V: (a) Conventional controller with load switched between half-load (R = 64 Ω) and full-load (R = 32 Ω), (b) Proposed controller with load switched between half-load (R = 64 Ω) and full-load (R = 32 Ω).

controllers when the primary side dc voltage V_1 is 250 V, and the load is switched between half-load and full-load. According to Fig. 8(a), when the load is jumped from half-load to full-load by using the conventional PI controller,

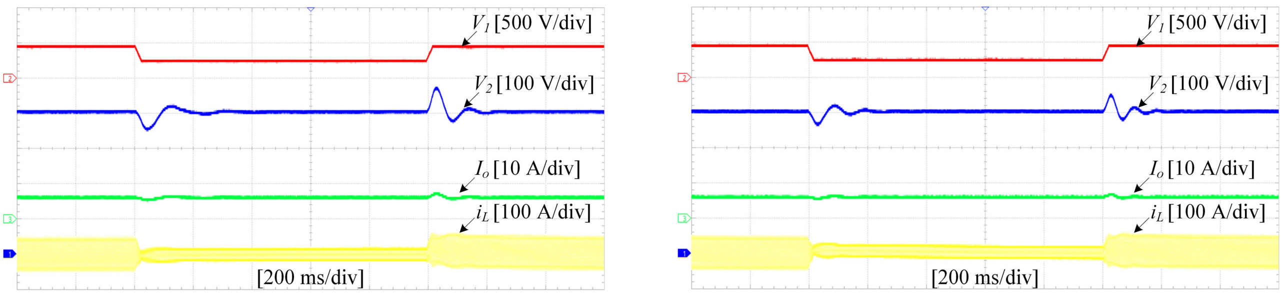

(a) (b)

FIGURE 10. **Dynamic-state experimental comparison of DAB converter under conventional and proposed controllers with half-load condition (R = 64 Ω) and primary side dc voltage switching between 250 V and 450 V: (a) Conventional controller, (b) Proposed controller.**

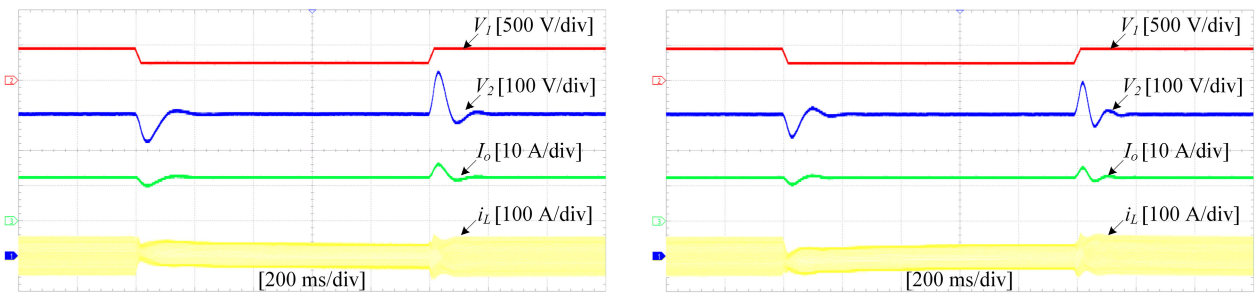

(a) (b)

FIGURE 11. **Dynamic-state experimental comparison of DAB converter under conventional and proposed controllers with full-load condition (R = 32 Ω) and primary side dc voltage switching between 250 V and 450 V: (a) Conventional controller, (b) Proposed controller.**

the secondary side dc voltage V_2 drops to 330 V, and the settling time takes almost 200 ms. However, as can be seen in Fig. 8(b), under the proposed controller, the experimental result shows satisfactory dynamic performances when switching between half-load and full-load, with slight voltage fluctuations and settling times.

Similar to Fig. 8, Fig. 9 shows the dynamic-state experimental comparison of the DAB converter under the conventional and proposed controllers while the primary side dc voltage V_1 is set to 450 V. As shown in Fig. 9(a), it is obvious that the secondary side dc voltage V_2 by using the conventional PI controller presents non-negligible voltage oscillations when the load varies, with a larger voltage fluctuation of 60 V and a longer settling time of 200 ms when the load is jumped from full-load to half-load. As a comparison in Fig. 9(b), the proposed controller shows excellent dynamic performances when switching between half-load and full-load, with negligible voltage fluctuations and settling times.

Fig. 10 and Fig. 11 show the dynamic-state experimental comparisons of the DAB converter under the conventional and proposed controllers with different load conditions and the change of primary side dc voltage. It can be seen that the effect of the proposed controller is mainly to reduce the amount of voltage fluctuation of the secondary side dc voltage V_2. Under the half-load condition, the voltage fluctuation of V_2 can be reduced by about 15 V when the primary side dc voltage V_1 is switched between 250 V and 450 V. Moreover, under the full-load condition, the voltage fluctuation of V_2 can be reduced by almost 20 V.

According to Fig. 8 to Fig. 11, it can be concluded that the proposed H∞ robust controller achieves better dynamic response than the conventional PI controller when load resistance jumps and primary side dc voltage variations. Furthermore, over the entire primary side dc voltage range of 250 V to 450 V, it indicates that the proposed H∞ robust controller can achieve system stability and robustness whenever half-load or full-load.

V. CONCLUSION

This paper presents the design of H∞ robust controller with load-current feed-forward for the DAB converter used in BESS. Based on DPS control, a polytopic model of the DAB converter with two uncertain elements is first established by convex optimization theory. LMIs are then used to design the H∞ robust controller conveniently to minimize the influence of disturbance on the output voltage. To ensure the dynamic performance of the system under a wide range of operating voltage conditions, a regional closed-loop pole configuration technique is properly adopted. To further enhance the dynamic response, an improved LCFF control with lookup tables for phase-shift compensation is investigated. A series of comparative experiment results obtained from a built OPAL-RT hard-ware-in-loop platform verify that the proposed H∞ robust controller achieves robust and fast dynamic performance.

As a future work, an experimental prototype with the same rated power will be designed to further verify the performance of the proposed H∞ robust controller. And the application of H∞ robust control can be extended to the DAB converter with TPS control or other power converters.

REFERENCES

[1] R. W. A. A. D. Doncker, D. M. Divan, and M. H. Kheraluwala, "A three-phase soft-switched high-power-density DC/DC converter for high-power applications," *IEEE Trans. Ind. Appl.*, vol. 27, no. 1, pp. 63–73, Jan. 1991, doi: 10.1109/28.67533.

[2] B. Zhao, Q. Song, W. Liu, and Y. Sun, "Overview of dual-active-bridge isolated bidirectional DC–DC converter for high-frequency-link power-conversion system," *IEEE Trans. Power Electron.*, vol. 29, no. 8, pp. 4091–4106, Aug. 2014, doi: 10.1109/TPEL.2013.2289913.

[3] T. Duong and S. Choi, "Deadbeat control with bivariate online parameter identification for SPS-modulated DAB converters," *IEEE Access*, vol. 10, pp. 54079–54090, 2022, doi: 10.1109/ACCESS.2022.3176428.

[4] X. Chen, J. Xu, and G. Xu, "Hybrid SPS control for ISOP dual-active-bridge converter based on modulated coupled inductor with full load range ZVS and RMS current optimization in DC transformer applications," *IEEE Access*, vol. 10, pp. 131394–131405, 2022, doi: 10.1109/ACCESS.2022.3227965.

[5] N. Hou and Y. Li, "Communication-free power management strategy for the multiple DAB-based energy storage system in islanded DC microgrid," *IEEE Trans. Power Electron.*, vol. 36, no. 4, pp. 4828–4838, Apr. 2021, doi: 10.1109/TPEL.2020.3019761.

[6] H. Akagi, S. Kinouchi, and Y. Miyazaki, "Bidirectional isolated dual-active-bridge (DAB) DC–DC converters using 1.2-kV 400-A SiC-MOSFET dual modules," *CPSS Trans. Power Electron. Appl.*, vol. 1, no. 1, pp. 33–40, Dec. 2016, doi: 10.24295/CPSSTPEA.2016.00004.

[7] K. Yu, F. Zhuo, F. Wang, X. Jiang, and Y. Gou, "MPC-based startup current shaping strategy with state-space model of DAB in DC distribution system," *IEEE J. Emerg. Sel. Topics Power Electron.*, vol. 10, no. 4, pp. 4073–4089, Aug. 2022, doi: 10.1109/JESTPE.2021.3138102.

[8] S. Park, J. W. Park, K. H. Kim, and F. Kang, "Battery energy storage system with interleaving structure of dual-active-bridge converter and non-isolated DC-to-DC converter with wide input and output voltage," *IEEE Access*, vol. 10, pp. 127205–127224, 2022, doi: 10.1109/ACCESS.2022.3226779.

[9] D. J. Almakhles, J. S. M. Ali, S. Padmanaban, M. S. Bhaskar, U. Subramaniam, and R. Sakthivel, "An original hybrid multilevel DC–AC converter using single-double source unit for medium voltage applications: Hardware implementation and investigation," *IEEE Access*, vol. 8, pp. 71291–71301, 2020, doi: 10.1109/ACCESS.2020.2986932.

[10] H. Bai, Z. Nie, and C. C. Mi, "Experimental comparison of traditional phase-shift, dual-phase-shift, and model-based control of isolated bidirectional DC–DC converters," *IEEE Trans. Power Electron.*, vol. 25, no. 6, pp. 1444–1449, Jun. 2010, doi: 10.1109/TPEL.2009.2039648.

[11] D. Segaran, D. G. Holmes, and B. P. McGrath, "Enhanced load step response for a bidirectional DC–DC converter," *IEEE Trans. Power Electron.*, vol. 28, no. 1, pp. 371–379, Jan. 2013, doi: 10.1109/TPEL.2012.2200505.

[12] W. Song, N. Hou, and M. Wu, "Virtual direct power control scheme of dual active bridge DC–DC converters for fast dynamic response," *IEEE Trans. Power Electron.*, vol. 33, no. 2, pp. 1750–1759, Feb. 2018, doi: 10.1109/TPEL.2017.2682982.

[13] W. Zhao, X. Zhang, S. Gao, and M. Ma, "Improved model-based phase-shift control for fast dynamic response of dual-active-bridge DC/DC converters," *IEEE J. Emerg. Sel. Topics Power Electron.*, vol. 9, no. 1, pp. 223–231, Feb. 2021, doi: 10.1109/JESTPE.2020.2972960.

[14] J. Sha, L. Chen, and G. Zhou, "Discrete extended-phase-shift control for dual-active-bridge DC–DC converter with fast dynamic response," *IEEE Trans. Ind. Electron.*, vol. 70, no. 6, pp. 5662–5673, Jun. 2023, doi: 10.1109/TIE.2022.3198261.

[15] T. Duong and S. Choi, "Sensor-reduction control for dual active bridge converter under dual-phase-shift modulation," *IEEE Access*, vol. 10, pp. 63020–63033, 2022, doi: 10.1109/ACCESS.2022.3182510.

[16] N. Hou, Y. Zhang, and Y. W. Li, "A load-current-estimating scheme with delay compensation for the dual-active-bridge DC–DC converter," *IEEE Trans. Power Electron.*, vol. 37, no. 3, pp. 2636–2647, Mar. 2022, doi: 10.1109/TPEL.2021.3111854.

[17] F. An, W. Song, K. Yang, N. Hou, and J. Ma, "Improved dynamic performance of dual active bridge DC–DC converters using MPC scheme," *IET Power Electron.*, vol. 11, no. 11, pp. 1756–1765, Sep. 2018, doi: 10.1049/iet-pel.2017.0707.

[18] D. Zhao, K. Shen, L. Chen, Z. Wang, W. Liu, T. Yang, and P. Wheeler, "Improved active damping stabilization of DAB converter interfaced aircraft DC microgrids using neural network-based model predictive control," *IEEE Trans. Transport. Electrific.*, vol. 8, no. 2, pp. 1541–1552, Jun. 2022, doi: 10.1109/TTE.2021.3094757.

[19] X. Meng, Y. Jia, Q. Xu, C. Ren, X. Han, and P. Wang, "A novel intelligent nonlinear controller for dual active bridge converter with constant power loads," *IEEE Trans. Ind. Electron.*, vol. 70, no. 3, pp. 2887–2896, Mar. 2023, doi: 10.1109/TIE.2022.3170608.

[20] Y. Zeng, A. I. Maswood, J. Pou, X. Zhang, Z. Li, C. Sun, S. Mukherjee, A. K. Gupta, and J. Dong, "Active disturbance rejection control using artificial neural network for dual-active-bridge-based energy storage system," *IEEE J. Emerg. Sel. Topics Power Electron.*, vol. 11, no. 1, pp. 301–311, Feb. 2023, doi: 10.1109/JESTPE.2021.3138341.

[21] L. Chen, S. Shao, Q. Xiao, L. Tarisciotti, P. W. Wheeler, and T. Dragicevic, "Model predictive control for dual-active-bridge converters supplying pulsed power loads in naval DC micro-grids," *IEEE Trans. Power Electron.*, vol. 35, no. 2, pp. 1957–1966, Feb. 2020, doi: 10.1109/TPEL.2019.2917450.

[22] L. Chen, L. Lin, S. Shao, F. Gao, Z. Wang, P. W. Wheeler, and T. Dragicevic, "Moving discretized control set model-predictive control for dual-active bridge with the triple-phase shift," *IEEE Trans. Power Electron.*, vol. 35, no. 8, pp. 8624–8637, Aug. 2020, doi: 10.1109/TPEL.2019.2962838.

[23] Y. Jeung and D. Lee, "Voltage and current regulations of bidirectional isolated dual-active-bridge DC–DC converters based on a double-integral sliding mode control," *IEEE Trans. Power Electron.*, vol. 34, no. 7, pp. 6937–6946, Jul. 2019, doi: 10.1109/TPEL.2018.2873834.

[24] N. Tiwary, V. Naik N, A. K. Panda, A. Narendra, and R. K. Lenka, "A robust voltage control of DAB converter with super-twisting sliding mode approach," *IEEE J. Emerg. Sel. Topics Ind. Electron.*, vol. 4, no. 1, pp. 288–298, Jan. 2023, doi: 10.1109/JESTIE.2022.3227007.

[25] P.-J. Ko and M.-C. Tsai, "H_∞ control design of PID-like controller for speed drive systems," *IEEE Access*, vol. 6, pp. 36711–36722, 2018, doi: 10.1109/ACCESS.2018.2851284.

[26] M. Yang, Y. Li, H. Du, C. Li, and Z. He, "Hierarchical multiobjective H-infinity robust control design for wireless power transfer system using genetic algorithm," *IEEE Trans. Control Syst. Technol.*, vol. 27, no. 4, pp. 1753–1761, Jul. 2019, doi: 10.1109/TCST.2018.2814589.

[27] L. Li, G. Pei, J. Liu, P. Du, L. Pei, and C. Zhong, "2-DOF robust H_∞ control for permanent magnet synchronous motor with disturbance observer," *IEEE Trans. Power Electron.*, vol. 36, no. 3, pp. 3462–3472, Mar. 2021, doi: 10.1109/TPEL.2020.3015874.

[28] Y. Liang, P. Sun, X. Wu, H. Zhou, J. Sun, G. Yang, J. Cai, and Q. Deng, "H_∞ robust control for ICPT system with selected weighting function considering parameter perturbations," *IEEE Trans. Power Electron.*, vol. 37, no. 11, pp. 13914–13929, Nov. 2022, doi: 10.1109/TPEL.2022.3179979.

[29] H. Ren and L. Ma, "H-infinity mixed sensitivity control of dual active bridge DC–DC converter," in *Proc. IEEE Int. Conf. Power, Intell. Comput. Syst. (ICPICS)*, Jul. 2021, pp. 16–20, doi: 10.1109/ICPICS52425.2021.9524165.

[30] C. Olalla, R. Leyva, A. E. Aroudi, P. Garces, and I. Queinnec, "LMI robust control design for boost PWM converters," *IET Power Electron.*, vol. 3, no. 1, pp. 75–85, Jan. 2010, doi: 10.1049/iet-pel.2008.0271.

[31] P. Xia, H. Shi, H. Wen, Q. Bu, Y. Hu, and Y. Yang, "Robust LMI-LQR control for dual-active-bridge DC–DC converters with high parameter uncertainties," *IEEE Trans. Transport. Electrific.*, vol. 6, no. 1, pp. 131–145, Mar. 2020, doi: 10.1109/TTE.2020.2975313.

[32] Q. Xiao, L. Chen, H. Jia, P. W. Wheeler, and T. Dragicevic, "Model predictive control for dual active bridge in naval DC microgrids supplying pulsed power loads featuring fast transition and online transformer current minimization," *IEEE Trans. Ind. Electron.*, vol. 67, no. 6, pp. 5197–5203, Jun. 2020, doi: 10.1109/TIE.2019.2934070.

[33] H. Bai and C. Mi, "Eliminate reactive power and increase system efficiency of isolated bidirectional dual-active-bridge DC–DC converters using novel dual-phase-shift control," *IEEE Trans. Power Electron.*, vol. 23, no. 6, pp. 2905–2914, Nov. 2008, doi: 10.1109/TPEL.2008.2005103.

[34] B. Zhao, Q. Song, W. Liu, and W. Sun, "Current-stress-optimized switching strategy of isolated bidirectional DC–DC converter with dual-phase-shift control," *IEEE Trans. Ind. Electron.*, vol. 60, no. 10, pp. 4458–4467, Oct. 2013, doi: 10.1109/TIE.2012.2210374.
[35] B. Zhao, Q. Song, and W. Liu, "Efficiency characterization and optimization of isolated bidirectional DC–DC converter based on dual-phase-shift control for DC distribution application," *IEEE Trans. Power Electron.*, vol. 28, no. 4, pp. 1711–1727, Apr. 2013, doi: 10.1109/TPEL.2012.2210563.
[36] F. An, W. Song, B. Yu, and K. Yang, "Model predictive control with power self-balancing of the output parallel DAB DC–DC converters in power electronic traction transformer," *IEEE J. Emerg. Sel. Topics Power Electron.*, vol. 6, no. 4, pp. 1806–1818, Dec. 2018, doi: 10.1109/JESTPE.2018.2823364.
[37] J. Bernussou, P. L. D. Peres, and J. C. Geromel, "A linear programming oriented procedure for quadratic stabilization of uncertain systems," *Syst. Control Lett.*, vol. 13, no. 1, pp. 65–72, Jul. 1989, doi: 10.1016/0167-6911(89)90022-4.
[38] S. Boyd, L. Ghaoui, E. Feron, and V. Balakrishnan, *Linear Matrix Inequality in Systems and Control Theory*. Philadelphia, PA, USA: SIAM Studies in Applied Mathematics, 1991.
[39] P. Gahinet and P. Apkarian, "A linear matrix inequality approach to H_∞ control," *Int. J. Robust Nonlinear Control*, vol. 4, no. 4, pp. 421–448, 1994, doi: 10.1002/rnc.4590040403.
[40] M. Chilali and P. Gahinet, "H_∞ design with pole placement constraints: An LMI approach," *IEEE Trans. Autom. Control*, vol. 41, no. 3, pp. 358–367, Mar. 1996, doi: 10.1109/9.486637.

XIAODONG XU was born in Gansu, China, in 1983. He received the B.S. and M.S. degrees from Xi'an Jiaotong University, Xi'an, China, in 2006 and 2010, respectively. He is currently pursuing the Ph.D. degree with the College of Electrical and Information Engineering, Lanzhou University of Technology, Lanzhou, China. Since 2012, he has been a Lecturer with the College of Energy and Power Engineering, Lanzhou University of Technology. His current research interests include pulse width modulation techniques and DC–DC converters.

GUANGQING BAO was born in China, in 1972. She received the Ph.D. degree in electrical engineering from Shanghai University, Shanghai, China, in 2006. She is currently a Professor with the School of Electrical Engineering and Information, Southwest Petroleum University, Chengdu, China. Her current research interests include special motor design, the integration of renewable energy into power systems, microgrid control and management, and renewable energy grid-connected control.

YUEWU WANG was born in Guangxi, China, in 1983. He received the Ph.D. degree in electrical engineering from the South China University of Technology, Guangzhou, China, in 2017. From 2017 to 2020, he was a Software Engineer with Shenzhen INVT Electric Company Ltd., Shenzhen, China. In 2020, he joined the School of Automation, Guangxi University of Science and Technology, Liuzhou, China, where he is currently a Lecturer. His current research interests include pulse width modulation techniques, DC–DC converters, and grid-connected inverters.

QIAN LI was born in China, in 1988. She received the Ph.D. degree in electrical engineering from Sichuan University, Chengdu, China. She is currently an Associate Professor with the School of Electrical Engineering and Information, Southwest Petroleum University, Chengdu. Her current research interests include power system stability and control, distributed generation, and integrated energy systems.